Electrochimica Acta 536 (2025) 146804

Contents lists available at ScienceDirect

Electrochimica Acta

journal homepage: www.journals.elsevier.com/electrochimica-acta

Enhanced photoelectrochemical glycerol oxidation with bismuth gradient $BiVO_4$ photoanodes

Martí Molera [a,b], Cristian Fàbrega [b,*], Maria Sarret [a], Teresa Andreu [a,*]

[a] SEP/IQTC, Departament de Ciència dels Materials i Química Física. Universitat de Barcelona (UB). Martí i Franquès 1, Barcelona, 08028, Spain
[b] MIND/IN2UB, Departament d'Enginyeria Electrònica i Biomèdica. Universitat de Barcelona (UB). Martí i Franquès 1, Barcelona, 08028, Spain

ARTICLE INFO

Keywords:
Photoelectrochemistry
Photoanode
$BiVO_4$
Electron transport layer
Glycerol oxidation

ABSTRACT

In this work, we propose a novel strategy for synthesizing $BiVO_4$ photoelectrodes for photocatalytic oxidation of glycerol. The two-step electrodeposition process of BiOI, followed by a thermal diffusion of vanadium, results in the formation of a $BiVO_4$ electrode with a bismuth gradient. This gradient leads to excess bismuth clusters at the FTO contact and a stoichiometric proportion at the electrode surface. Structural, optical, and photoelectrochemical characterization revealed that the bismuth gradient acts as an electron transport layer, with superior photoelectrochemical properties in comparison to unmodified $BiVO_4$. This includes lower electron/hole recombination, while maintaining its glycerol oxidation catalytic properties.

1. Introduction

In recent years, there has been an increased focus on the production of green hydrogen, given its potential as an energy vector to replace fossil fuels. Consequently, there has been a rise in interest in water splitting, as it can produce hydrogen with renewable energy sources. However, the electrolysis of water is energy-intensive due to the sluggish kinetics of the oxygen evolution reaction (OER), which results in a high overpotential [1]. To overcome these limitations, a strategy that has been proposed is the replacement of OER by the oxidation of organic compounds with faster kinetics, with the aim of reducing the energy consumption [2].

Glycerol, a by-product of biodiesel production [3,4], has demonstrated significant potential as a cost-effective alternative to the OER. In this context, glycerol not only reduces energy consumption by acting as a cheap feedstock, but also enhances the economic viability of the anodic reaction by producing high added value products such as dihydroxyacetone and formic acid [5,6]. However, there are two key challenges that must be addressed for wider industry adoption: reducing overall energy costs and enhancing the selectivity towards a single compound to minimize separation costs.

In recent studies, researchers have proposed the use of semiconductor electrodes to power the process with solar light. Titanium oxide has been the most widely studied semiconductor for glycerol oxidation (GOR), but its high affinity for OER results in low selectivity. Additionally, its large bandgap (3.2 eV) limits the solar absorption [7–9]. Alternatively, tungsten oxide (WO_3) offers high resistance to photocorrosion and stability in acidic conditions [10,11] along with a suitable band gap for absorbing a wider portion of the solar spectrum. Despite the advantages of WO_3, bismuth vanadate ($BiVO_4$) is a stronger candidate for glycerol oxidation due to its low bandgap (2.4 eV) and suitable conduction band edges for both OER and GOR [12–14]. However, the poor electronic transport properties of $BiVO_4$ result in a high recombination rate of photogenerated charge carriers, which reduces its overall photoelectrochemical output [15]. Numerous strategies have been attempted to improve $BiVO_4$ performance by either introducing a co-catalyst on the surface to enhance the GOR [16–23] or incorporating an electron transport layer to enhance charge extraction [24–26]. The Bi:V stoichiometric ratio also significantly influences the performance of $BiVO_4$ photoanodes and some studies have shown that V and Bi vacancies at the electrode surface can modify band alignment [13,27–30] affecting interfacial charge transfer [31].

This work presents a novel strategy for synthesizing $BiVO_4$ with a graded Bi:V stoichiometric ratio, resulting in superior photoelectrochemical properties. Our comprehensive characterization of the $BiVO_4$ photoelectrodes revealed that bismuth excess at the FTO interface acts as an electron transport layer, improving charge extraction at the back contact.

* Corresponding authors.
E-mail addresses: cfabrega@ub.edu (C. Fàbrega), tandreu@ub.edu (T. Andreu).

https://doi.org/10.1016/j.electacta.2025.146804
Received 21 February 2025; Received in revised form 5 June 2025; Accepted 29 June 2025
Available online 30 June 2025

2. Experimental

2.1. Synthesis of photoanodes

In the present study, $BiVO_4$ photoelectrodes have been prepared using four different strategies, as shown in Fig. 1. Conventional $BiVO_4$ photoanodes have been prepared by the well-stablished electrodeposition of BiOI (step A), followed by a thermal diffusion of vanadium (step B_1). In this work, we propose a two-step electrodeposition process of BiOI with an intermediate thermal conversion of BiOI to Bi_2O_3 (step B_2) prior to the thermal diffusion of V to promote the formation of a bismuth rich interface with the conductive substrate (G-$BiVO_4$). For comparison, photoanodes were prepared with the two-step electrodeposition process of BiOI but without the thermal conversion to Bi_2O_3 (2x$BiVO_4$), as well as $BiVO_4$ derived from Bi_2O_3 (ox-$BiVO_4$). The detailed preparation of the photoanodes is described below.

2.1.1. $BiVO_4$ synthesis

The $BiVO_4$ photoelectrodes were synthesized using a two-step process: electrodeposition followed by thermal treatment [32]. First, BiOI was electrodeposited onto FTO-coated glass (7 Ω sq^{-1}, Sigma-Aldrich) substrates using two sequential potentiostatic pulses: −0.35 V vs Ag/AgCl/KCl (3.5 M) for 1 min followed by −0.1 V vs Ag/AgCl/KCl (3.5 M) for 3 min. The electrochemical bath consisted of 0.97 g of $Bi(NO_3)_3$ (reagent grade, Acros organics) and 3.32 g of KI (99 %, Panreac) in 50 mL of water. Once the reagents had been dissolved, a solution of 0.12 g of p-benzoquinone (reagent grade, Fisher Chemical) in 20 mL of ethanol (96 %, Panreac) was added. After electrodeposition, the resulting BiOI electrodes were rinsed with deionized water and air-dried. Then, a drop of vanadium precursor solution was deposited onto each electrode. The vanadium precursor solution consisted of a dimethyl sulfoxide (DMSO) (99.9 %, Sigma-Aldrich) solution with 0.2 M vanadyl acetylacetonate (99 %, Acros organics). The electrodes were then heated at 450 °C for 2 h with a heating ramp of 2 °C min^{-1}. After cooling, excess V_2O_5 was removed by rinsing with a 1 M KOH (pellets for analysis, Sulpelco) solution for 3 min.

2.1.2. G-$BiVO_4$ synthesis

To synthesize the G-$BiVO_4$ electrodes (where G denotes a gradient), a BiOI layer was first electrodeposited onto FTO-coated glass substrates using the same conditions as described previously. These electrodes were then heated at 550 °C for 2 h with a heating ramp of 2 °C min^{-1} to obtain a Bi_2O_3 layer. A second BiOI layer was electrodeposited and finally, the electrode was thermally treated with the vanadium precursor at 450 °C for 2 h with a heating ramp of 2 °C min^{-1}. After cooling, excess V_2O_5 was removed by rinsing with a 1 M KOH solution for 3 min.

2.1.3. 2x-$BiVO_4$ synthesis

To synthesize the 2x-$BiVO_4$, two identical BiOI layer were sequentially electrodeposited onto FTO-coated glass substrates using the same conditions as previously described, followed by a second identical electrodeposition. The resulting electrodes were then thermally treated with the vanadium precursor, following the $BiVO_4$ synthesis method. After cooling, excess V_2O_5 was removed by rinsing with a 1 M KOH solution for 3 min.

2.1.4. Ox-$BiVO_4$ synthesis

The Ox-$BiVO_4$ electrodes were synthesized by electrodepositing a BiOI layer onto FTO-coated glass substrates, utilizing the same conditions as previously described. These electrodes were then heated at 550 °C for 2 h with a heating ramp of 2 °C min^{-1} to obtain a Bi_2O_3 layer. Finally, the electrode was thermally treated with the vanadium precursor at 450 °C for 2 h with a heating ramp of 2 °C min^{-1}. After cooling, excess V_2O_5 was removed by rinsing with a 1 M KOH solution for 3 min.

2.2. Structural characterization

The morphology of the $BiVO_4$ electrodes was analyzed using a JEOL J-7100 field emission scanning electron microscopy (FESEM) coupled with energy dispersive spectroscopy (EDS). X-ray diffraction (XRD) spectra were acquired using a PANalytical X'pert PRO diffractometer with monochromatized CuKα radiation (λ = 1.5406 Å), operating at 45 kV and 40 mA in a Bragg-Brentano configuration. Raman spectroscopy was conducted using a Jovin Yvon LabRaman HR800 in the 100 – 1000 cm^{-1} range employing three different lasers (325, 532 and 785 nm) and calibrated with a silicon reference. UV–vis spectroscopy (UV–vis) was performed on a Lambda 950 UV–vis-NIR spectrometer (PerkinElmer) equipped with a 150 mm Integrating Sphere and Spectralon standard.

2.3. Photoelectrochemical characterization

Photoelectrochemical measurements were made in a 4 × 1 × 1 cm^3 Hellma optical glass cuvette using a three-electrode configuration. An Ag/AgCl/KCl (3.5 M) served as the reference electrode, and a platinum filament as the counter electrode. A Newport LSH-7320 solar simulator was used to illuminate the samples from both the frontside (electrolyte-electrode interface, EE) and back side (substrate-electrode interface, SE). Incident Photon-Electron Conversion Efficiency (IPCE) measurements were conducted at 1 V_{RHE} using band pass filters (Thorlabs) with 10 nm bandwidth, ranging from 400 to 540 nm. The electrolyte used was 0.5 M Na_2SO_4 with 0.1 M glycerol at pH 2. IPCE was calculated using Eq. (1), where λ is the wavelength, j_{light} is the measured photocurrent under each illumination condition, j_{dark} is the dark current, and P is the incident light power density measured with a silicon photodiode (Thorlabs

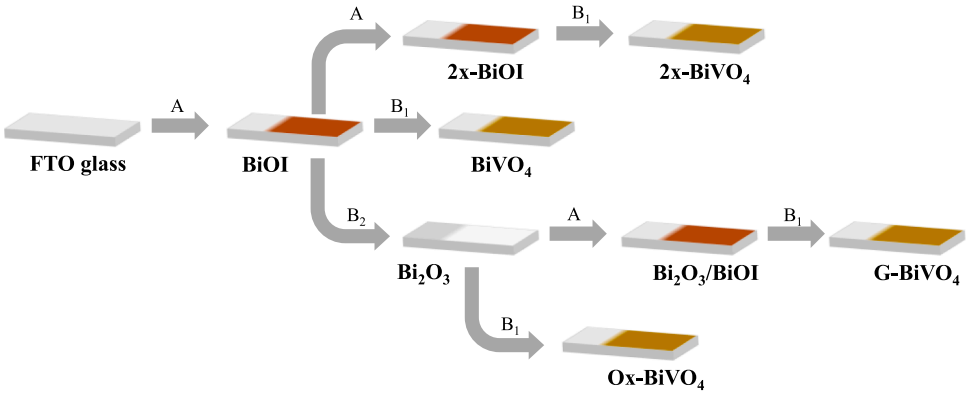

Fig. 1. $BiVO_4$, 2x-$BiVO_4$, G-$BiVO_4$, and Ox-$BiVO_4$ synthesis scheme. A corresponds to the electrodeposition step at −0.35 V_{AgCl} for 1 min and −0.1 V_{AgCl} for 3 min. B_1 corresponds to the vanadium precursor thermal treatment step at 450 °C for 2 h followed by the V_2O_5 removal with KOH. B_2 corresponds to the thermal treatment step at 550 °C for 2 h.

S120VC).

$$IPCE = \frac{\left(\frac{1240}{\lambda} \cdot (j_{light} - j_{dark}\right)}{P} \cdot 100 \quad (1)$$

Mott-Schottky measurements were done under dark conditions in a 0.5 M Na_2SO_4 (99 %, Merck) electrolyte at pH 2 for OER and with the addition of 0.1 M glycerol (99.5 %, VWR chemicals) for GOR. All measurements were carried out at a frequency of 1000 Hz.

Photocurrent transient measurements were performed at 1 V_{RHE} under 1 sun illumination with chopped light. The electrolyte used was 0.5 M Na_2SO_4 at pH 2 for OER and the same electrolyte with the addition of 0.1 M glycerol for GOR. The j_{ss}/j_o ratio was calculated, where j_0 is the initial current density when the illumination is turned on, and j_{ss} is the current density just before the illumination is turned off, when the electrode has reached a steady state. The ratio j_{ss}/j_o gives an approximation of the charge carrier recombination rate within the electrode. A ratio closer to 1 indicates less recombination.

2.4. Glycerol photoelectrolysis

The photoelectrochemical oxidation of glycerol was studied in a home-made two-compartment Teflon electrochemical cell (3 mL volume) equipped with an optical glass window [7]. A Nafion 117 membrane separated the two compartments, and the same three-electrode cell configuration was employed.

The analysis of glycerol oxidation products was carried out in 0.5 M Na_2SO_4 and 0.1 M glycerol electrolyte at a constant potential of 1 V_{RHE} under 1 sun illumination until a charge of 2.5 C mL^{-1} had passed (Table S1). After electrolysis, the sample was kept at 12 °C and analyzed by high-performance liquid chromatography (HPLC) and proton nuclear magnetic resonance (^{1}H NMR).

HPLC analysis has been done with a Waters Alliance 2695 chromatograph with an Aminex HPLX-87H carboxylic acid column maintained at 60 °C. The mobile phase consisted of 10 mM sulfuric acid with a flow rate of 0.6 mL min^{-1} and an injection volume of 100 μL. The products were detected with a Jasco UV-1570 UV–vis spectrophotometer and a RID, Waters 2414 refraction index detector.

The ^{1}H NMR analysis was performed in a Bruker 400 spectrometer with a water suppression method. For sample preparation, 490 μL of the sample was mixed with 20 μL of 0.2 %vol DMSO and 90 μL of deuterated water.

Faradaic efficiency (FE) was calculated using the concentration of products (mol l^{-1}) obtained from HPLC and ^{1}H NMR analysis. The equation used to calculate FE is:

$$FE\ (\%) = \frac{c\ z\ F}{Q} \cdot 100 \quad (2)$$

Where c is the concentration of the desired product (mol l^{-1}), z is the number of electrons exchanged in the electrooxidation reaction (Equations S1-S4), F is the Faraday constant (95,485 C mol^{-1}) and Q is the total charge passed during the electrolysis (C l^{-1}).

3. Discussion

3.1. Structural characterization

FESEM images (Fig. 2) illustrate the morphologies of the electrodes at different stages of the synthesis. The initial BiOI deposit exhibits a needle-like morphology (Fig. 2a), which evolves into a worm-like structure with large isolated fragments upon thermal treatment (Fig. 2b).

Further XRD analysis (Fig. S1) confirmed the complete transformation of BiOI to Bi_2O_3 after the thermal treatment and revealed that the Bi_2O_3 layer consists of a mixture of the α, β and γ phases. The thermal

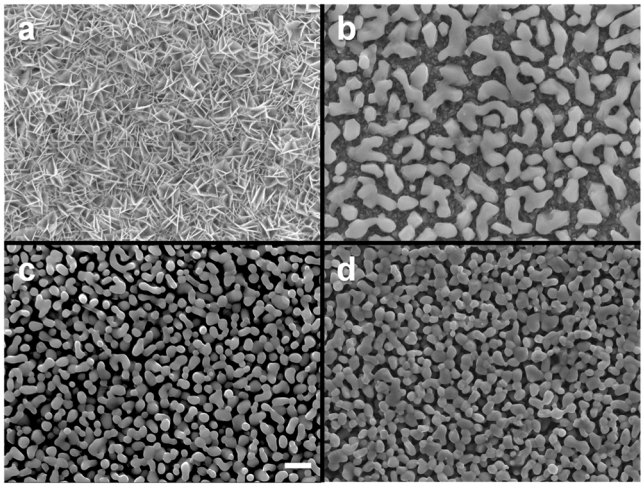

Fig. 2. FESEM images of (a) BiOI, (b) Bi_2O_3, (c) G-$BiVO_4$ and (d) $BiVO_4$. Scale bar corresponds to 1 μm.

treatment of BiOI with the vanadium precursor resulted in the formation of a $BiVO_4$ with a similar morphology, albeit with smaller and interconnected fragments (Fig. 2d). Fig. 2c shows that G-$BiVO_4$ has the same structure and grain size as $BiVO_4$, indicating that the intermediate layer of Bi_2O_3 formed during the synthesis does not affect the final surface morphology. XRD analysis (Fig. S1) confirmed the complete transformation of the BiOI and Bi_2O_3 layers into a continuous $BiVO_4$ phase. In the cross section of the G-$BiVO_4$ (Fig. 3), two distinct layers are visible: the bottom layer corresponding to the FTO of the substrate and the upper layer corresponding to the $BiVO_4$. EDS analysis (Table S2) shows that the Bi:V ratio is approximately 1:1 in both electrodes. However, cross-sectional analysis (Fig. S2 and Table S3) shows an excess of bismuth near the FTO contact. This difference in the stoichiometric ratio between the electrode surface and the FTO contact suggests the presence of a bismuth gradient within the G-$BiVO_4$ electrode.

Raman spectroscopy (Fig. 4a) confirmed the presence of monoclinic $BiVO_4$, as evidenced by characteristic bands at 826 cm^{-1}, 365 cm^{-1}, 326 cm^{-1}, 208 cm^{-1} and 126 cm^{-1} [33–35]. The band at 826 cm^{-1} corresponds to the symmetric V-O stretching mode (Ag). The bands at 365 cm^{-1} and 326 cm^{-1} are attributed to the symmetric (Ag) and antisymmetric (Bg) V-O bending modes of VO_4 tetrahedra, respectively. Finally, the bands at 208 cm^{-1} and 126 cm^{-1} are associated with the external rotation and translation modes. The G-$BiVO_4$ electrode exhibits two additional bands at 178 cm^{-1} and 187 cm^{-1}, which can be attributed to either metallic bismuth (Bi^0) or α-Bi_2O_3. But the absence of other α-Bi_2O_3 peaks (282 cm^{-1} and 410 cm^{-1}) confirms that it corresponds to metallic bismuth [36–38]. This indicates that there is the formation of small bismuth

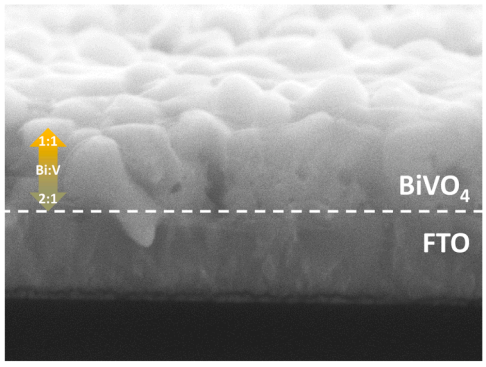

Fig. 3. G-$BiVO_4$ FESEM transversal section. Yellow arrow represents the Bi:V proportion alongside the material.

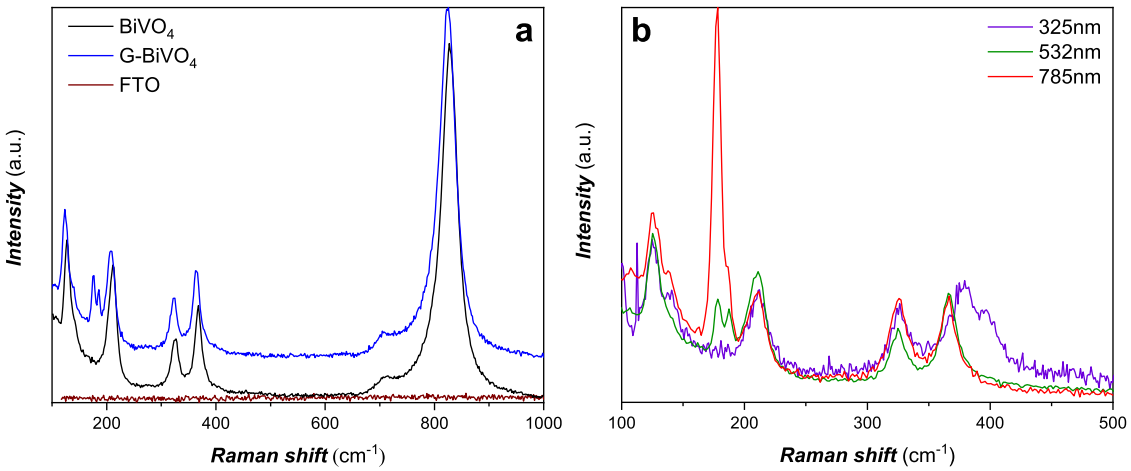

Fig. 4. (a) Raman spectra at 532 nm incident wavelength of the $BiVO_4$ and G-$BiVO_4$ electrodes. (b) Raman spectra of the G-$BiVO_4$ electrode at 325, 532 and 785 nm incident wavelengths.

clusters within the $BiVO_4$ structure. The Raman spectra of the Ox-$BiVO_4$ (synthesized by applying a vanadium thermal treatment to a Bi_2O_3 electrode) show the same peaks as those of the G-$BiVO_4$ (Fig. S3). This corroborates that the Bi_2O_3 layer can transform into $BiVO_4$, leading to the formation of bismuth clusters.

To investigate the depth profile of the bismuth clusters, we conducted additional Raman measurements using different excitation wavelengths (325 nm and 785 nm) which probe different depths within the electrode. As shown in Fig. 4b, the intensity of the peaks at 178 cm^{-1} and 187 cm^{-1} increases in the deeper layers of the G-$BiVO_4$ electrode, while they disappear at the surface. At the lower excitation wavelength (325 nm), which has a shallower penetration depth, the G-$BiVO_4$ electrode shows an identical Raman spectrum to the $BiVO_4$ electrode (Fig. S4). This indicates that the surface of the G-$BiVO_4$ electrode has the same structure as that of the $BiVO_4$ electrode. However, the increased intensity of the Bi^0 peaks at greater depths suggests higher concentration bismuth clusters within the G-$BiVO_4$ electrode. The XRD patterns in Fig. S5 confirm that both the $BiVO_4$ and G-$BiVO_4$ structures match the monoclinic $BiVO_4$ (JCPDS 00–014–0688), with no detectable metallic bismuth phase. This indicates that the bismuth clusters are amorphous.

The combined results of EDS, Raman spectroscopy, and XRD analyses confirm the successful synthesis of a $BiVO_4$ electrode with a graded bismuth concentration. The Bi:V ratio is stoichiometric at the surface, while a bismuth-rich region, composed of bismuth clusters, exists near the FTO contact. These clusters are formed during the thermal treatment step, as illustrated in Fig. 5. During this step, the vanadium (IV) of the precursor is oxidized to vanadium (V) and atmospheric oxygen is reduced to produce the vanadate ion. In the case of $BiVO_4$ and 2x-$BiVO_4$ synthetic routes, since BiOI is porous, all the material can be converted to $BiVO_4$. However, the Bi_2O_3 layer is more compact, resulting in areas with limited O_2 accessibility. This leads to the reduction of the bismuth (III) to metallic bismuth, forming the clusters.

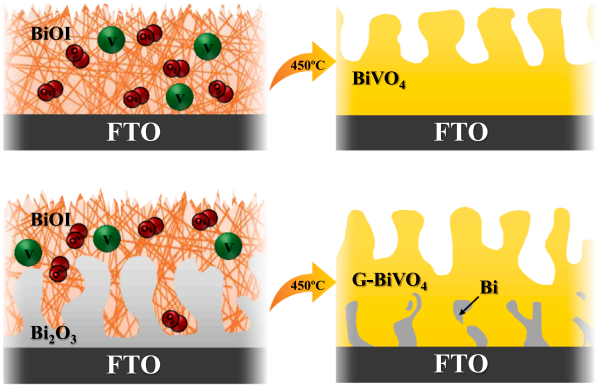

Fig. 5. Diagram of the bismuth clusters formation upon vanadium thermal treatment.

UV–vis analysis (Fig. S6) was employed to determine the bandgaps of the G-$BiVO_4$ and $BiVO_4$ electrodes, which were found to be 2.3 eV and 2.4 eV, respectively. The bandgap of the Bi_2O_3 layer was also determined to be 2.7 eV, which is similar to the reported values of the α-Bi_2O_3 phase [39,40].

3.2. Photoelectrochemical characterization

Fig. 6 illustrates the linear sweep voltammograms of the electrodes under both back (SE) and front (EE) illumination conditions in the absence and presence of 0.1 M glycerol. The G-$BiVO_4$ electrode presents superior performance for the oxygen evolution reaction (OER) compared to the $BiVO_4$ electrode under both illumination conditions. In back illumination, the onset potentials for $BiVO_4$ and G-$BiVO_4$ are 0.93 V_{RHE} and 0.66 V_{RHE}, respectively. Under front illumination, the onset potentials are 0.90 V_{RHE} and 0.57 V_{RHE}, respectively. At 1 V_{RHE}, the G-

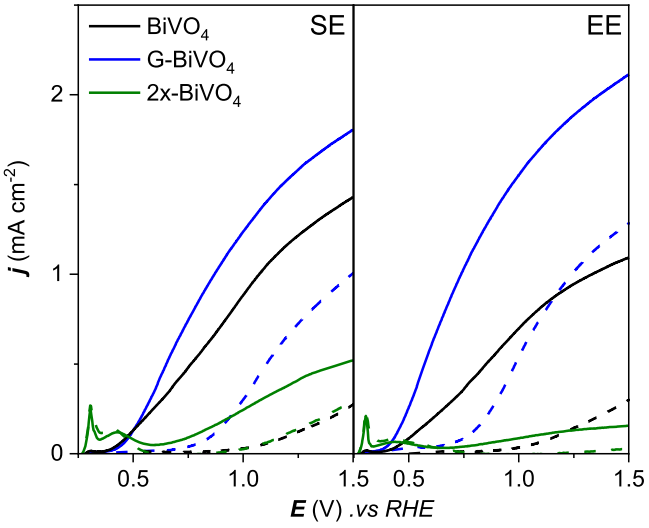

Fig. 6. LSV curves recorded at a scan rate of 5 mV s^{-1} in Na_2SO_4 0.5 M electrolyte pH 2 for OER (dotted line) and with added 0.1 M glycerol for GOR (full line) conditions, under 1 sun illumination. Measurements were done under back (SE) and front (EE) illumination.

$BiVO_4$ electrode achieves current densities of 0.27 mA cm^{-2} and 0.53 mA cm^{-2} for back and front illumination, respectively. In contrast, the $BiVO_4$ electrode does not exceed 0.05 mA cm^{-2} under either illumination condition.

For the glycerol oxidation (GOR), the G-$BiVO_4$ electrode also presents improved performance, achieving higher photocurrents at 1 V_{RHE}. Specifically, it achieves current densities of 1.15 mA cm^{-2} and 1.55 mA cm^{-2} under back and front illumination, respectively. In comparison, the $BiVO_4$ electrode yields photocurrents of 0.88 mA cm^{-2} and 0.7 mA cm^{-2} under back and front illumination, respectively. Despite the improved performance of G-$BiVO_4$, there are minimal differences in onset potential between the G-$BiVO_4$ and the $BiVO_4$ electrodes, with both exhibiting an onset potential around 0.4 V_{RHE}, regardless of the illumination conditions. The photovoltage of each electrode was calculated from the difference between the light and dark OCV measurements and is presented in Table S4. For the OER, the G-$BiVO_4$ electrode presents a photovoltage of 0.26 V, compared to 0.16 V for the $BiVO_4$ electrode. For the GOR, the photovoltages are 0.52 V and 0.37 V, respectively. This is consistent with the improved photoelectrochemical (PEC) properties observed for the G-$BiVO_4$ electrode. The higher photovoltage suggests improved charge separation, possibly due to a reduction in surface defects. This enhancement in light harvesting is also reflected in the IPCE measurements (Fig. S7). At 460 nm, the IPCE for the G-$BiVO_4$ electrode (30.5 %) is double that of the $BiVO_4$ electrode (15.5 %). To confirm that the improved PEC performance is not simply due to an increase in $BiVO_4$ layer thickness, a control $BiVO_4$ electrode was synthesized with double the BiOI electrodeposition time (2x-$BiVO_4$). As can be seen in Fig. 6 and Table S5, this thicker electrode has significantly lower PEC performance. This is attributed to the higher recombination rate inherent in thicker $BiVO_4$ layers, which reduces the overall PEC performance [41].

To further characterize the surface photoelectrochemical properties, we conducted Mott-Schottky measurements on both the G-$BiVO_4$ and the $BiVO_4$ electrodes. We extracted the charge carrier density (N_d) and the flat band potential (V_{fb}) from the Mott-Schottky plots (Fig. S8 and summarized them in Table S6). The positive slope confirms that $BiVO_4$ is an n-type semiconductor. A comparison of the values obtained in the sulfate electrolyte with and without glycerol reveals no significant variation in either N_d or V_{fb}, suggesting that glycerol addition does not significantly affect the band bending of either G-$BiVO_4$ or $BiVO_4$ electrodes. We obtained N_d values for both electrodes ($4{\cdot}10^{19}$ cm^{-3} and $2{\cdot}10^{19}$ cm^{-3} for G-$BiVO_4$ and $BiVO_4$, respectively) that are consistent with those reported in the literature [42,43]. The G-$BiVO_4$ electrode exhibits a V_{fb} of 0.85 V_{RHE}, while the $BiVO_4$ electrode has a V_{fb} of 0.91 V_{RHE}. These lower V_{fb} values for the G-$BiVO_4$ electrode suggest that its Fermi level is closer to the conduction band, which is consistent with its higher charge carrier density.

A comparison of the photocurrent under front and back illumination (Fig. 6) reveals that the G-$BiVO_4$ electrode achieves higher photocurrent under front illumination, while the $BiVO_4$ electrode performs better under back illumination. This indicates that the $BiVO_4$ electrode suffers from a higher recombination rate due to poor charge transport. To further investigate this, we conducted photocurrent transient measurements in the presence (GOR) and absence (OER) of glycerol, using in the Na_2SO_4 and Na_2SO_4 + glycerol electrolytes, respectively (Fig. 7 and Fig. S9). For the OER, the G-$BiVO_4$ electrode exhibits a lower recombination rate (j_{ss}/j_0 = 0.90) compared to the $BiVO_4$ electrode (j_{ss}/j_0 = 0.55), confirming that the $BiVO_4$ electrode suffers from a higher combination rate. For the GOR, both electrodes exhibit a j_{ss}/j_0 ratio of 1. This is because glycerol acts as a hole scavenger, effectively preventing charge accumulation on the surface.

We also conducted LSV measurements at neutral pH (Fig. S10). As expected, a decrease in current density was observed compared to acidic conditions. This is consistent with previous reports indicating that glycerol adsorption is favored under acidic conditions, resulting in enhanced charge transfer [5]. These results further support the conclusion that the Bi gradient in the G-$BiVO_4$ electrode plays a beneficial role

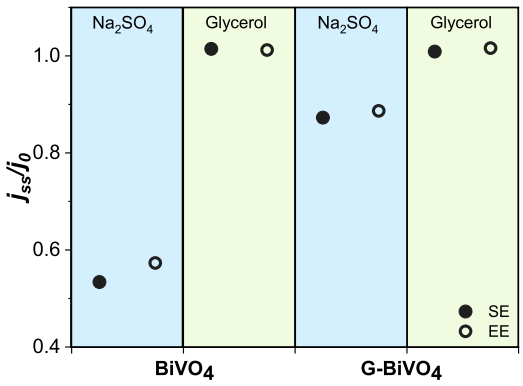

Fig. 7. J_{ss} and J_0 relation obtained from chronoamperometries at 1 V_{RHE}, in Na_2SO_4 0.5 M electrolyte pH 2 for OER (blue) and with added 0.1 M glycerol for GOR (green) conditions, under chopped 1 sun illumination. Measurements were done under back (SE) and front (EE) illumination.

in charge carrier dynamics. In addition to the observed increase in photocurrent and reduced recombination, these features can be rationalized by considering the electronic structure modulation introduced by the Bi gradient.

Mechanistically, the Bi gradient in G-$BiVO_4$ introduces a favorable band structure across the electrode thickness. The increasing bismuth concentration toward the FTO substrate likely creates a built-in electric field, facilitating directional transport of photogenerated electrons toward the back contact while promoting hole migration to the surface. This internal potential gradient reduces bulk recombination, as evidenced by the higher j_{ss}/j_0 ratio and improved photovoltage. Furthermore, the presence of metallic Bi clusters near the FTO may contribute to a local reduction in the work function, enhancing band alignment with the conductive substrate and improving electron injection efficiency. This effect is consistent with the improved photocurrent response under back illumination and the lower onset potential for the oxygen evolution reaction.

These features align with previous studies where compositional or doping gradients within semiconductor photoelectrodes have been shown to improve charge separation and transport by inducing spatial band bending or forming graded heterojunctions [26,29]. In our system, the Bi-rich region acts synergistically as an internal electron transport layer and as a contact modifier, without compromising the catalytic surface composition.

3.3. *Photoelectrochemical glycerol valorization*

Photoelectrochemical glycerol valorization measurements were conducted at 1 V_{RHE} since it is the potential at which the $BiVO_4$ electrodes does not have a significant oxygen evolution contribution. As shown in Fig. S11, both the $BiVO_4$ and the G-$BiVO_4$ exhibit good long-term stability during photoelectrolysis, particularly under acidic conditions. Fig. 8 presents the faradaic efficiencies towards glycerol oxidation products using $BiVO_4$ and G-$BiVO_4$ electrodes. These products are grouped into three categories: C1 products consisting on formic acid (FA), C2 products consisting on glycolaldehyde (GOAD), and C3 products consisting on glyceric acid (GLA), glyceraldehyde (GLAD) and dihydroxyacetone (DHA). $BiVO_4$ electrodes show an evenly distribution between products categories, with a 25 % for C1, a 20 % for C2 and a 25 % for C3 products. Within the C3 category, dihydroxyacetone and glyceraldehyde are predominant, with a small presence of glyceric acid.

When comparing product distribution for $BiVO_4$ under acidic and neutral conditions, only minor differences are observed. Acidic conditions slightly enhance C3 product formation, while neutral conditions favor glycolaldehyde production. Additionally, acidic conditions promote dihydroxyacetone formation, whereas neutral pH promote

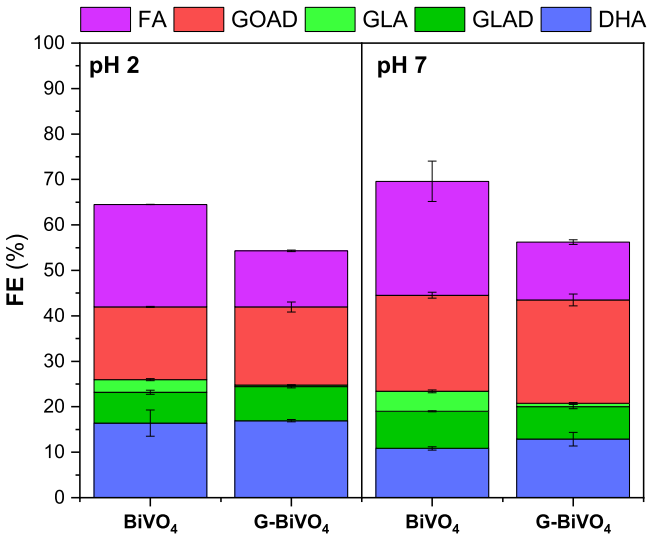

Fig. 8. Faradaic efficiency of the glycerol oxidation products from the electrolysis at 1 V_{RHE}. Determined products: Formic acid (FA), glycolaldehyde (GOAD), glyceric acid (GLA), glyceraldehyde (GLAD) and dihydroxyacetone (DHA).

glyceraldehyde formation, likely due to the tautomerization equilibrium being shifted by the pH difference [44]. Because of that, the main difference between the two conditions is the electrolysis time required to reach the same charge. Under acidic conditions, higher currents are achieved, allowing the same charge to be reached much faster, as shown in Table S1.

The G-$BiVO_4$ electrode produces the same products as the $BiVO_4$ electrode, suggesting that the Bi gradient does not significantly alter the electrocatalytic reaction pathways. However, a slight reduction in the faradaic efficiency can be observed. This decrease could result from either overoxidation to CO_2 or increased competition from the OER. Voltammograms in Fig. 6 show that the G-$BiVO_4$ has a non-negligible photocurrent at the working potential (1V_{RHE}) in the absence of glycerol, which initially suggests enhanced OER competition. However, a closer analysis of individual product faradaic efficiencies reveals that only formic and glyceric acids exhibit reduced faradaic efficiencies, whereas all the other products remain unchanged. If OER were primarily responsible, a uniform decrease across all products would be expected. Therefore, the observed loss in faradaic efficiency is more likely due to overoxidation to CO_2, driven by the enhanced kinetics of G-$BiVO_4$. Despite this slight reduction in liquid products due to increased CO_2 production, the G-$BiVO_4$ electrode remains highly selective for glycerol oxidation, exhibiting minor competition with the OER.

4. Conclusions

In this work, we successfully synthesized a Bi-rich $BiVO_4$ using a simple electrodeposition method which generated a Bi cluster gradient, transitioning from a 2:1 Bi:V stoichiometry at the FTO contact to a 1:1 stoichiometry at the electrode surface. The presence of this Bi gradient improved charge separation and reduced electron-hole recombination by acting as an electron transport layer. As a result, the G-$BiVO_4$ electrode exhibited an enhanced photocurrent density, reaching 1.15 mA cm^{-2} and 1.55 mA cm^{-2} for glycerol oxidation at 1 V vs RHE under back and front illumination conditions, respectively. Importantly, maintaining a 1:1 stoichiometry at the electrode surface ensured that the G-$BiVO_4$ electrode retained the same selectivity for glycerol oxidation products as the bare $BiVO_4$ electrode.

Declaration of competing interest

The authors declare that they have no known competing financial interests or personal relationships that could have appeared to influence the work reported in this paper.

Acknowledgments

The financial support from Ministerio de Ciencia e Innovación and FEDER-UE through project PID2022–138491OB-C33 (MICIU/AEI/10.13039/501100011033) and from AGAUR Generalitat de Catalunya (2021SGR00712, 2024 FI-1 00421) are gratefully acknowledged. Authors thank Centres Científics I Tecnològics (CCiTUB), Universitat de Barcelona for the expert and technical help on, Raman, FESEM, HPLC and ^{1}H NMR techniques and to Dr. Julià Lopez Vidrier the access to the UV–vis equipment.

Supplementary materials

Supplementary material associated with this article can be found, in the online version, at doi:10.1016/j.electacta.2025.146804.

References

[1] M.G. Walter, E.L. Warren, J.R. McKone, S.W. Boettcher, Q. Mi, E.A. Santori, N. S. Lewis, Solar water splitting cells, Chem. Rev. 110 (2010) 6446–6473, https://doi.org/10.1021/cr1002326.
[2] M.T. Bender, X. Yuan, K.-S. Choi, Alcohol oxidation as alternative anode reactions paired with (photo)electrochemical fuel production reactions, Nat Commun 11 (2020) 4594, https://doi.org/10.1038/s41467-020-18461-1.
[3] T. Attarbachi, M.D. Kingsley, V. Spallina, New trends on crude glycerol purification: a review, Fuel 340 (2023) 127485, https://doi.org/10.1016/j.fuel.2023.127485.
[4] T. Kahlstorf, J.N. Hausmann, T. Sontheimer, P.W. Menezes, Challenges for hybrid water electrolysis to replace the oxygen evolution reaction on an industrial scale, Global Challenges 7 (2023) 2200242, https://doi.org/10.1002/gch2.202200242.
[5] D. Liu, J.-C. Liu, W. Cai, J. Ma, H.B. Yang, H. Xiao, J. Li, Y. Xiong, Y. Huang, B. Liu, Selective photoelectrochemical oxidation of glycerol to high value-added dihydroxyacetone, Nat Commun 10 (2019) 1779, https://doi.org/10.1038/s41467-019-09788-5.
[6] L. Wen, X. Zhang, F.F. Abdi, Photoelectrochemical glycerol oxidation as a sustainable and valuable technology, Materials Today Energy (2024) 101648, https://doi.org/10.1016/j.mtener.2024.101648.
[7] M. Molera, M. Sarret, C. Fàbrega, Effect of light and electrode polarization on BiVO $_4$ and TiO $_2$ photoanodes for glycerol oxidation, J. Electrochem. Soc. 171 (2024) 086503, https://doi.org/10.1149/1945-7111/ad6bc3.
[8] S. Çetinkaya, G. Khamidov, L. Özcan, L. Palmisano, S. Yurdakal, Selective photoelectrocatalytic oxidation of glycerol by nanotube, nanobelt and nanosponge structured TiO2 on Ti plates, Journal of Environmental Chemical Engineering 10 (2022) 107210, https://doi.org/10.1016/j.jece.2022.107210.
[9] L. Luo, W. Chen, S.-M. Xu, J. Yang, M. Li, H. Zhou, M. Xu, M. Shao, X. Kong, Z. Li, H. Duan, Selective photoelectrocatalytic glycerol oxidation to dihydroxyacetone via enhanced middle hydroxyl adsorption over a Bi $_2$ O $_3$ -incorporated catalyst, J. Am. Chem. Soc. 144 (2022) 7720–7730, https://doi.org/10.1021/jacs.2c00465.
[10] M.B. Costa, M.A. De Araújo, M.V.D.L. Tinoco, J.F.D. Brito, L.H. Mascaro, Current trending and beyond for solar-driven water splitting reaction on WO3 photoanodes, Journal of Energy Chemistry 73 (2022) 88–113, https://doi.org/10.1016/j.jechem.2022.06.003.
[11] J. Yu, J. González-Cobos, F. Dappozze, F.J. López-Tenllado, J. Hidalgo-Carrillo, A. Marinas, P. Vernoux, A. Caravaca, C. Guillard, WO3-based materials for photoelectrocatalytic glycerol upgrading into glyceraldehyde: unravelling the synergistic photo- and electro-catalytic effects, Applied Catalysis B: Environmental 318 (2022) 121843, https://doi.org/10.1016/j.apcatb.2022.121843.
[12] F.F. Abdi, L. Han, A.H.M. Smets, M. Zeman, B. Dam, R. Van De Krol, Efficient solar water splitting by enhanced charge separation in a bismuth vanadate-silicon tandem photoelectrode, Nat Commun 4 (2013) 2195, https://doi.org/10.1038/ncomms3195.
[13] A. Venugopal, R. Kas, K. Hau, W.A. Smith, Operando infrared spectroscopy reveals the dynamic nature of semiconductor–Electrolyte interface in multinary metal oxide photoelectrodes, J. Am. Chem. Soc. 143 (2021) 18581–18591, https://doi.org/10.1021/jacs.1c08245.
[14] L.-W. Huang, T.-G. Vo, C.-Y. Chiang, Converting glycerol aqueous solution to hydrogen energy and dihydroxyacetone by the BiVO4 photoelectrochemical cell, Electrochim. Acta 322 (2019) 134725, https://doi.org/10.1016/j.electacta.2019.134725.
[15] L. Li, X. Yang, Y. Lei, H. Yu, Z. Yang, Z. Zheng, D. Wang, Ultrathin Fe-NiO nanosheets as catalytic charge reservoirs for a planar Mo-doped BiVO $_4$ photoanode, Chem. Sci. 9 (2018) 8860–8870, https://doi.org/10.1039/C8SC03297A.

[16] X. Lu, K. Ye, S. Zhang, J. Zhang, J. Yang, Y. Huang, H. Ji, Amorphous type FeOOH modified defective BiVO4 photoanodes for photoelectrochemical water oxidation, Chemical Engineering Journal 428 (2022) 131027, https://doi.org/10.1016/j.cej.2021.131027.
[17] H. Tateno, S.-Y. Chen, Y. Miseki, T. Nakajima, T. Mochizuki, K. Sayama, Photoelectrochemical oxidation of glycerol to dihydroxyacetone over an acid-resistant Ta:biVO $_4$ Photoanode, ACS Sustainable Chem. Eng. 10 (2022) 7586–7594, https://doi.org/10.1021/acssuschemeng.2c01282.
[18] M.A. De Araújo, D. Coelho, L.H. Mascaro, E.C. Pereira, The iron oxyhydroxide role in the mediation of charge transfer for water splitting using bismuth vanadate photoanodes, J Solid State Electrochem 22 (2018) 1539–1548, https://doi.org/10.1007/s10008-017-3774-1.
[19] D.A. Reddy, Y. Kim, H.S. Shim, K.A.J. Reddy, M. Gopannagari, D.Praveen Kumar, J.K. Song, T.K. Kim, Significant improvements on BiVO $_4$ @CoPi Photoanode solar water splitting performance by extending visible-light harvesting capacity and charge carrier transportation, ACS Appl. Energy Mater. 3 (2020) 4474–4483, https://doi.org/10.1021/acsaem.0c00169.
[20] Y.-H. Wu, D.A. Kuznetsov, N.C. Pflug, A. Fedorov, C.R. Müller, Solar-driven valorisation of glycerol on BiVO $_4$ photoanodes: effect of co-catalyst and reaction media on reaction selectivity, J. Mater. Chem. A 9 (2021) 6252–6260, https://doi.org/10.1039/D0TA10480A.
[21] B. He, F. Zhao, P. Yi, J. Huang, Y. Wang, S. Zhao, Z. Li, Y. Zhao, X. Liu, Spinel-oxide-integrated BiVO $_4$ photoanodes with photothermal effect for efficient solar water oxidation, ACS Appl. Mater. Interfaces 13 (2021) 48901–48912, https://doi.org/10.1021/acsami.1c15225.
[22] M. Zhao, T. Chen, B. He, X. Hu, J. Huang, P. Yi, Y. Wang, Y. Chen, Z. Li, X. Liu, Photothermal effect-enhanced photoelectrochemical water splitting of a BiVO $_4$ photoanode modified with dual-functional polyaniline, J. Mater. Chem. A 8 (2020) 15976–15983, https://doi.org/10.1039/D0TA03698F.
[23] Y. Han, M. Chang, Z. Zhao, F. Niu, Z. Zhang, Z. Sun, L. Zhang, K. Hu, Selective valorization of glycerol to formic acid on a BiVO $_4$ photoanode through NiFe phenolic networks, ACS Appl. Mater. Interfaces 15 (2023) 11678–11690, https://doi.org/10.1021/acsami.2c20516.
[24] L.-P. Li, M. Liu, W.-D. Zhang, Electrodeposition of CdS onto BiVO4 films with high photoelectrochemical performance, J Solid State Electrochem 22 (2018) 2569–2577, https://doi.org/10.1007/s10008-018-3973-4.
[25] P.M. Rao, L. Cai, C. Liu, I.S. Cho, C.H. Lee, J.M. Weisse, P. Yang, X. Zheng, Simultaneously efficient light absorption and charge separation in WO $_3$ /BiVO $_4$ core/Shell Nanowire Photoanode for photoelectrochemical water oxidation, Nano Lett 14 (2014) 1099–1105, https://doi.org/10.1021/nl500022z.
[26] S. Lee, J. Song, Y.-R. Jo, K.S. Choi, J. Lee, S. Seo, T.L. Kim, H.W. Jang, C. Jeon, B.-J. Kim, B. Kim, S. Lee, In situ growth of nanostructured BiVO $_4$ –Bi $_2$ O $_3$ mixed-phase via nonequilibrium deposition involving metal exsolution for enhanced photoelectrochemical water splitting, ACS Appl. Mater. Interfaces 11 (2019) 44069–44076, https://doi.org/10.1021/acsami.9b12916.
[27] D. Lee, W. Wang, C. Zhou, X. Tong, M. Liu, G. Galli, K.-S. Choi, The impact of surface composition on the interfacial energetics and photoelectrochemical properties of BiVO4, Nat Energy 6 (2021) 287–294, https://doi.org/10.1038/s41560-021-00777-x.
[28] Q. Wang, Z. Wang, N. Liao, S. Montilla-Verdú, M. Contreras, N. Guijarro, J. Luo, Tailoring the surface termination of BiVO $_4$ photoanodes using ammonium metavanadate enhances the solar water oxidation performance, ACS Energy Lett 9 (2024) 3308–3315, https://doi.org/10.1021/acsenergylett.4c01240.
[29] Y. Lu, Y. Yang, X. Fan, Y. Li, D. Zhou, B. Cai, L. Wang, K. Fan, K. Zhang, Boosting charge transport in BiVO $_4$ photoanode for solar water oxidation, Advanced Materials 34 (2022) 2108178, https://doi.org/10.1002/adma.202108178.
[30] T. Tran-Phu, Z. Fusco, I. Di Bernardo, J. Lipton-Duffin, C.Y. Toe, R. Daiyan, T. Gengenbach, C.-H. Lin, R. Bo, H.T. Nguyen, G.M.J. Barca, T. Wu, H. Chen, R. Amal, A. Tricoli, Understanding the role of vanadium vacancies in BiVO $_4$ for efficient photoelectrochemical water oxidation, Chem. Mater. 33 (2021) 3553–3565, https://doi.org/10.1021/acs.chemmater.0c04866.
[31] A.M. Hilbrands, S. Zhang, C. Zhou, G. Melani, D.H. Wi, D. Lee, Z. Xi, A.R. Head, M. Liu, G. Galli, K.-S. Choi, Impact of varying the photoanode/catalyst interfacial composition on solar water oxidation: the case of BiVO $_4$ (010)/FeOOH photoanodes, J. Am. Chem. Soc. 145 (2023) 23639–23650, https://doi.org/10.1021/jacs.3c07722.
[32] K.J. McDonald, K.-S. Choi, A new electrochemical synthesis route for a BiOI electrode and its conversion to a highly efficient porous BiVO4 photoanode for solar water oxidation, Energy Environ. Sci. 5 (2012) 8553, https://doi.org/10.1039/c2ee22608a.
[33] H.M. Zhang, J.B. Liu, H. Wang, W.X. Zhang, H. Yan, Rapid microwave-assisted synthesis of phase controlled BiVO4 nanocrystals and research on photocatalytic properties under visible light irradiation, J Nanopart Res 10 (2008) 767–774, https://doi.org/10.1007/s11051-007-9310-y.
[34] G. Li, Y. Bai, W.F. Zhang, Difference in valence band top of BiVO4 with different crystal structure, Mater Chem Phys 136 (2012) 930–934, https://doi.org/10.1016/j.matchemphys.2012.08.023.
[35] J. Yu, A. Kudo, Effects of structural variation on the photocatalytic performance of hydrothermally synthesized BiVO $_4$, Adv Funct Materials 16 (2006) 2163–2169, https://doi.org/10.1002/adfm.200500799.
[36] J.A. Steele, R.A. Lewis, In situ micro-Raman studies of laser-induced bismuth oxidation reveals metastability of β-Bi_2O_3 microislands, Opt. Mater. Express 4 (2014) 2133, https://doi.org/10.1364/OME.4.002133.
[37] K. Trentelman, A note on the characterization of bismuth black by Raman microspectroscopy, J Raman Spectroscopy 40 (2009) 585–589, https://doi.org/10.1002/jrs.2184.
[38] O. Depablos-Rivera, A. Martínez, S.E. Rodil, Interpretation of the Raman spectra of bismuth oxide thin films presenting different crystallographic phases, J Alloys Compd 853 (2021) 157245, https://doi.org/10.1016/j.jallcom.2020.157245.
[39] L. Leontie, M. Caraman, M. Delibaş, G.I. Rusu, Optical properties of bismuth trioxide thin films, Mater Res Bull 36 (2001) 1629–1637, https://doi.org/10.1016/S0025-5408(01)00641-9.
[40] V. Fruth, M. Popa, D. Berger, R. Ramer, M. Gartner, A. Ciulei, M. Zaharescu, Deposition and characterisation of bismuth oxide thin films, J Eur Ceram Soc 25 (2005) 2171–2174, https://doi.org/10.1016/j.jeurceramsoc.2005.03.025.
[41] K.R. Tolod, S. Hernández, M. Castellino, F.A. Deorsola, E. Davarpanah, N. Russo, Optimization of BiVO4 photoelectrodes made by electrodeposition for sun-driven water oxidation, Int J Hydrogen Energy 45 (2020) 605–618, https://doi.org/10.1016/j.ijhydene.2019.10.236.
[42] Q. Shi, S. Murcia-López, P. Tang, C. Flox, J.R. Morante, Z. Bian, H. Wang, T. Andreu, Role of tungsten doping on the surface states in BiVO $_4$ photoanodes for water oxidation: tuning the electron trapping process, ACS Catal 8 (2018) 3331–3342, https://doi.org/10.1021/acscatal.7b04277.
[43] X. Wu, F.E. Oropeza, S. Chang, M. Einert, Q. Wu, C. Maheu, J. Gallenberger, C. Tian, K. Lv, J.P. Hofmann, Promoting effect of interfacial hole accumulation on photoelectrochemical water oxidation in BiVO4 and Mo doped BiVO4, Advanced Powder Materials (2024) 100234, https://doi.org/10.1016/j.apmate.2024.100234.
[44] L. Cheng, C. Doubleday, R. Breslow, Evidence for tunneling in base-catalyzed isomerization of glyceraldehyde to dihydroxyacetone by hydride shift under formose conditions, Proc. Natl. Acad. Sci. U.S.A. 112 (2015) 4218–4220, https://doi.org/10.1073/pnas.1503739112.